INTEGRATION OF INFRASONIC MODELS WITH OCEAN WAVE SPECTRA AND ATMOSPHERIC SPECIFICATIONS TO PRODUCE GLOBAL ESTIMATES OF MICROBAROM SIGNAL LEVELS

Milton A. Garcés, Claus H. Hetzer, Mark Willis, and Steven Businger

University of Hawaii, Manoa

Sponsored by Defense Threat Reduction Agency

Contract No. DTRA01-01-C-0077

ABSTRACT

Severe weather in the ocean generates infrasonic signals in the 0.1-0.5 Hz frequency band that can propagate for thousands of kilometers. The source generation mechanism for these microbarom signals is attributed to the nonlinear interaction of surface ocean waves, which are predicted to radiate acoustically only if the swells are almost opposite in direction and of a near identical frequency. We study the statistics of microbarom signals detected at International Monitoring System (IMS) station I59US, Hawaii, to identify features that may be used to assess array performance in the microbarom range. For selected storm systems, we use the global ocean wave estimates produced by National Oceanic and Atmospheric Administration's (NOAA's) Wavewatch 3 (WW3) to estimate the spatial and temporal distribution of the acoustic source spectra induced by nonlinear ocean wave interactions. We then use empirical amplitude scaling relationships to predict microbarom signal levels and peak frequencies. Results are presented with a view toward applications in storm and sea-state evolution and how these affect infrasonic detection thresholds in the microbarom frequency band.

OBJECTIVE

The aim of this work is to characterize microbarom signals observed in the Pacific and model the source processes that generate these signals, with the aim of determining infrasonic detection thresholds in the microbarom frequency range.

RESEARCH ACCOMPLISHED

1. Introduction

Microbaroms consist of atmospheric pressure oscillations with energy between 0.1 and 1 Hz and a peak at ~0.2 Hz, and they can appear as coherent energy bursts or as a continuous oscillation. For infrasonic stations near the ocean, microbarom clutter often defines the low-wind noise floor, and thus detection thresholds, in that band. Like their seismic and hydroacoustic counterpart (microseisms), microbaroms are associated with severe weather in the ocean (Benioff and Gutenberg, 1939; Rind, 1980), and more specifically, to the ocean swells generated during storms (Posmentier, 1967; Kibblewhite and Wu, 1996, Garcés et al, 2002). We use the theoretical microbarom generation model of Arendt and Fritts (2000) with the third-generation Wavewatch 3 (WW3) ocean wave model of Tolman et al (2002) to try to reproduce our observations of microbarom signals at I59US.

2. Observations and theoretical background

Infrasound array I59US, Hawaii, has four elements and a baseline of ~2km. It was believed that microbaroms would be incoherent across this larger aperture. Although in general the continuous microbarom noise is indeed uncorrelated, distinct microbarom packets can be clearly detected in Hawaii. When designing an array it would perhaps be useful to retain the coherence of microbaroms, as then it may be possible to remove this contribution from a signal of interest.

The microbarom field at I59US varies seasonally and generally follows the yearly pattern for severe weather in the Pacific. In summer most of the microbaroms appear to come from the east and south, and in winter they arrive from the north and west. Statistics for microbarom signals for year 2002 are discussed in Garcés and Hetzer 2002. According to theory (e.g. Arendt and Fritts, 2000), microbaroms can be generated by ocean surface waves propagating with nearly the same period and the opposite direction. However, a real developed sea consists of multiple frequency and direction components, and on any given point in the central Pacific there may be between 4 and 7 swells interacting with each other. We choose to use the WW3 model of Tolman et al. (2003) because it provides reliable estimates of the ocean wave field directional spectrum that we can use as an excitation function for our microbarom amplitude estimates.

2.1. Ocean wave spectrum

The WW3 model outputs the variance density, F, of the surface wave field as a function of frequency, f, and propagation direction, θ, at each node of a global 1 degree grid. At each point of that grid, the variance density can be integrated over angle and frequency to provide the total wave energy E,

$$E = \int_0^{2\pi} d\theta \int_0^{\infty} df F(f,\theta). \quad (1)$$

The significant wave height is defined as

$$H_s = 4\sqrt{E}. \quad (2)$$

And thus the variance density has units of m^2/(rad*Hz) and it is a measure of the energy in the surface wave field. The phase of each wave component is assumed to be random. Figure 1 shows an example of the significant wave height and dominant period of the global surface wave field. However, these plots show the average of the ocean wave field after integration over frequency and angle, whereas we need the variance density itself to produce estimates of the microbarom pressure field.

Arendt and Fritz (2000) start with a prescribed amplitude spectrum of the ocean surface wave field given by the cosine Fourier transform

$$g(x,y,t) = \int_{-\infty}^{\infty} dk_x \int_{-\infty}^{\infty} dk_y A(k_x,k_y)\cos(\omega t - k_x x - k_y y + \phi) \tag{3}$$

$$= \int_{-\infty}^{\infty} dk_x \int_{-\infty}^{\infty} dk_y A(k_x,k_y)\cos(\omega t - k_x x - k_y y + \phi)$$

Thus we wish to find a functional relationship between the variance density F (also known as the directional spectrum) and the Fourier coefficient A, which has to have units of m^3.

From Kinsman (1965), Eq. (8.3:1)

$$g(x,y,t) = \int_0^{\infty} \int_{-\pi}^{\pi} \cos(\omega t - k_x x - k_y y + \phi)\sqrt{F(\omega,\theta)d\theta d\omega} \tag{4}$$

This integral representation reminds us that we are dealing with a Gaussian process, and is the subject of a detailed discussion by Kinsman. Since the WW3 model is defined in a grid of frequencies and azimuths, we estimate our wavenumber spectrum as:

$$g(x,y,t) \approx \int_0^{\infty} \int_{-\pi}^{\pi} \cos(\omega t - k_x x - k_y y + \phi)\sqrt{\frac{F(\omega,\theta)}{\Delta\theta\Delta\omega}}d\theta d\omega$$

The first transformation only concerns the change of variables from frequency to wavenumber,

$$g(x,y,t) \approx \int_0^{\infty} \int_{-\pi}^{\pi} \cos(\omega t - k_x x - k_y y + \phi)\frac{d\omega}{dk}\sqrt{\frac{F(\omega,\theta)}{\Delta\theta\Delta\omega}}d\theta dk \tag{5}$$

$$g(x,y,t) \approx \int_0^{\infty} \int_{-\pi}^{\pi} \cos(\omega t - k_x x - k_y y + \phi)c_g\sqrt{\frac{F(\omega,\theta)}{\Delta\theta\Delta\omega}}d\theta dk$$

where c_g is the group velocity. The second transformation involves a change of coordinates in wavenumber space from polar to rectangular,

$$g(x,y,t) \approx \int_{-\infty}^{\infty} dk_x \int_{-\infty}^{\infty} dk_y \cos(\omega t - k_x x - k_y y + \phi)\frac{c_g}{k}\sqrt{\frac{F(\omega,\theta)}{\Delta\theta\Delta\omega}} \tag{6}$$

For short-period waves, the phase velocity c_s and group velocity c_g are given as

$$c_s = \frac{\omega}{k} = \sqrt{\frac{g}{k}} = \frac{g}{\omega}, \quad c_g = \frac{1}{2}c_s, \tag{7}$$

and the dispersion relation is $\omega^2 = gk$. Comparison of Eq.(6) with Eq.(3) yields

$$A(k_x,k_y) = \frac{c_g}{k}\sqrt{\frac{F(k_x,k_y)}{\Delta\theta\Delta\omega}} \tag{8}$$

Since the variables in the radical have units of (m s), we see that A has units of m^3, as desired.

2.2. Acoustic spectrum

From Arendt and Fritts (2000) the pressure field radiated by a three dimensional surface wave field into an isotropic half space may be expressed as

$$p_m(x,y,z,t) = \int_{-\infty}^{\infty} dK_x \int_{-\infty}^{\infty} dK_y \int_{0}^{\infty} dK_z P_k(K_x, K_y, K_z) \exp\left(\omega_m t - \vec{K} \bullet \vec{R} + \phi\right) \tag{9}$$

where K is the acoustic wavenumber, ω_m is the angular frequency for the sound field, and R is the spherical radius from the source location to the receiver. The spectrum P_k is given by

$$P_k = \frac{\rho c^6}{64 g^2} K_z K^4 \int_0^{2\pi} A(k_x, k_y) A(k'_x, k'_y) d\theta_\xi \tag{10}$$

where k and k' correspond to the second order, propagating solutions of interacting wave fields with near equal angular frequencies ω and ω' and opposite directions, and

$$\begin{aligned} K^2 &= K_x^2 + K_y^2 + K_z^2 \\ K_x &= k_x + k'_x,\ \xi_x = k_x - k'_x \\ K_y &= k_y + k'_y,\ \xi_y = k_y - k'_y \\ K_z &= \sqrt{\left(\frac{\omega + \omega'}{c}\right)^2 - K_x^2 - K_y^2}\ . \end{aligned} \tag{11}$$

The highest spectral amplitude will occur when $K_x = K_y = 0$, or $k' = -k$, and $\omega = \omega'$, and

$$P_k^0 = \frac{\rho c^6}{64 g^2} K^5 \int_0^{2\pi} A(k_x, k_y) A(-k_x, -k_y) d\theta \tag{12}$$

$$\begin{aligned} \xi_x &= 2k_x \\ \xi_y &= 2k_y \\ K = K_z &= \frac{2\omega}{c} = \frac{\omega_m}{c}. \end{aligned} \tag{13}$$

Where θ is now the directional angle for k specified in equation (1). Using Equations (6) and (8), as well as $\omega_m = 2\omega$,

$$A(k_x, k_y) A(-k_x, -k_y) = \left(\frac{c_g}{k}\right)^2 \frac{\sqrt{F(k_x, k_y) F(-k_x, -k_y)}}{\Delta\theta \Delta\omega} = \left(\frac{4g^2}{\omega_m^3}\right)^2 \frac{\sqrt{F(k_x, k_y) F(-k_x, -k_y)}}{\Delta\theta \Delta\omega}\ . \tag{14}$$

The peak microbarom source spectrum amplitude then becomes

$$P_k^0 = \frac{\rho c g^2}{4\omega_m \Delta\theta \Delta\omega} \left[\int_0^{2\pi} \sqrt{F(k_x, k_y) F(-k_x, -k_y)} d\theta \right] = \frac{\rho c g^2}{4\omega_m (\Delta\theta \Delta\omega)} Q_m^0 \tag{15}$$

$$Q_m^0 = \int_0^{2\pi} \sqrt{F(k_x, k_y) F(-k_x, -k_y)} d\theta = 2 \int_0^{\pi} \sqrt{F(f, \theta) F(f, \theta + \pi)} d\theta \tag{16}$$

The integral can be readily evaluated through either the trapezoidal rule or the parabolic rule. For an even number of intervals n (odd number of discrete points x_j, $j = 0,n$), the parabolic rule states

$$\int_a^b f(x)dx \approx \frac{h}{3}\left[f(x_0)+4f(x_1)+2f(x_2)+...+4f(x_{n-1})+f(x_n)\right], \tag{17}$$

where $h = (b-a)/n$. If n is an odd number (even number of points), we can use the trapezoidal rule

$$\int_a^b f(x)dx \approx \frac{h}{2}\left[f(x_0)+2f(x_1)+2f(x_2)+...+2f(x_{n-1})+f(x_n)\right]. \tag{18}$$

After this integration is complete, we have completed the transformation from ocean to sound waves. For the evaluation of the sound field it is practical to use the acoustic microbarom angular frequency $\omega_m = 2\omega$.

2.3. Pressure scaling with range, including the effects of the stratospheric winds

The atmosphere is a complex propagation medium, and for the purpose of microbarom amplitude determinations it behooves us to start with a simple amplitude scaling relationship that will allow us to estimate relative acoustic levels at a receiver. Stevens et al (2002) provide an evaluation of various scaling laws that have been derived from nuclear tests, and we use the expression that provided the best fit:

$$P = \frac{P_{ref}}{R^{1.36}} 10^{0.019v} \tag{19}$$

where the reference pressure P_{ref} is relative to the source location, the range R is in km, and the stratospheric wind speed v at 50 km along the propagation direction is given in m/s. For our initial tests we ignore the stratospheric winds, which will be eventually incorporated using Naval Research Laboratory (NRL) ground-to-space (G2S) atmospheric specifications. A source magnitude may be defined as

$$M_I = log_{10}(P_{ref}), \tag{20}$$

and used to plot the microbarom source spectrum amplitude as a function of global location.

3. Implementation and Results

Figure 2 shows a graphical user interface developed for the computation of the infrasonic field generated by a specified ocean wavefield. The upper panel shows the microbarom source pressure corresponding to the swell plots in Figure 1 at a microbarom frequency of 0.2 Hz, which corresponds to an ocean wave frequency of 0.1 Hz. As noted earlier, the significant wave height plots are derived from an integral over all angles and frequencies (Equations 1 and 2), although the WW3 model output provides the directional spectrum of the ocean wavefield at each grid point. Thus the upper panel of Figure 2 was produced by taking the base 10 logarithm of Equation 15, which yields a frequency dependent source pressure spectrum at each grid point. To propagate the sound field, we need to specify a threshold magnitude below which we ignore source contributions. We also specify a range mask, after which we do not propagate the source point any further. To compute the lower panel of Figure 2, we ignored source points with magnitudes lower than –1 and propagated to 180 degrees away from the source, or to the antipode. To compute the propagated field shown in the lower panel of Figure 2, we compute the distance from each source point with a magnitude greater than –1 and within 180 degrees to the receiver. A dual processor SunBlade workstation takes ~8 hours to run this model. For this algorithm, the speed of computation depends on the source threshold that is used. A more realistic (and computationally expensive) model would also produce a propagation time from the source to the receiver, so that for each time step of the wave model there would actually be a series of time-lagged acoustic solutions. When we include the stratospheric winds as well as attenuation, we need to consider in more detail each source-receiver path. Time dependence and integration with atmospheric models will be incorporated into later generations of the computational algorithm.

Figure 2 only shows the results at a microbarom frequency of 0.2 Hz. It is also possible to look at the peak pressure and peak frequency of the source and received field, as shown in Figure 3. We see that the received field is richer in lower frequencies, and that higher microbarom noise levels are expected in sites that are close to the ocean. At each

grid point we can extract the acoustic source and received fields, and Figure 4 shows the spectra for a grid point at 20N, 160W. Comparison with the observed spectrum at I59US (lower panel of Figure 4) shows that despite our sweeping assumptions and generalizations, we have a reasonable match between theory and observation. The predicted peak frequency appears lower than the observed frequency, and this discrepancy may be corrected by accounting for the acoustic radiation pattern of the ocean wave interactions. Adding a viscous attenuation term may reduce the higher frequency components. These promising results encourage further development of the computational algorithm.

CONCLUSIONS AND RECOMMENDATIONS

The algorithm described in this paper is designed to produce a proof of concept integration of oceanographic and acoustic models, and the next level of detail should incorporate atmospheric specifications as well as more accurate acoustic radiation and propagation models. However, these improvements will require far more computational power than can be presently provided by desktop computers. During the next stage of the project, we would port the WW3 model to the Maui High Performance Computing Center Linux Supercluster. The acoustic propagation algorithm should include the atmospheric winds, attenuation, and the propagation time of the signals. The microbarom source mechanism needs to incorporate the radiation pattern of the microbarom source instead of considering only the peak power. The WW3 model needs to be modified so as to include reflections at coastlines and bathymetry changes, and could also be extended into a lower frequency. Our preliminary results are encouraging, and should eventually permit the generation of temporally and spatially dependent microbarom noise levels that may be used to compute more realistic global detection thresholds for IMS infrasound stations. Conversely, infrasonic observations may be used to refine ocean wave models in regions of poor coverage.

REFERENCES

Arendt, S. and D. Fritts (2000), Acoustic Radiation by Ocean Surface Waves, *Journal of Fluid Mechanics* 415, 1-21.

Benioff, H. and B. Gutenberg (1939), Waves and Currents Recorded by Electromagnetic Barographs*, Bulletin of the American Meteorological Society* 20, 421.

Garcés, M. and C. Hetzer (2003). Optimizing the Progressive Multi-Channel Correlation Detector for the Discrimination of Infrasonic Sources, 25th Seismic Research Review, this proceedings.

Garcés, M. and C. Hetzer (2002), "Evaluation of infrasonic detection algorithms," in "Proceedings of the 24th Seismic Research Review, Nuclear Explosion Monitoring: Innovation and Integration," (Ponte Vedra, FL) Los Alamos National Laboratory document LA-UR-02-5048 (September 2002).

Garcés, M., C. Hetzer, S. Businger, and M. Willis, "Modeling of microbarom signals in the pacific," in "Proceedings of the 24th Seismic Research Review, Nuclear Explosion Monitoring: Innovation and Integration," (Ponte Vedra, FL) Los Alamos National Laboratory document LA-UR-02-5048 (September 2002).

Kibblewhite, A., and C. Y. Wu (1996), Wave Interactions as a Seismo-Acoustic Source *Lecture Notes in Earth Sciences*, Springer-Verlag, Berlin.

Kinsman, B. (1965), *Wind Waves*, Prentice Hall, N.J., USA.

Posmentier, E. (1967), A Theory of Microbaroms, *Geophysical Journal of the Royal Astronomical Society* 13, 487.

Rind, D. (1980), Microseisms and Palisades 3. Microseisms and Microbaroms, *Journal of Geophysical Research* 85, 4854.

Stevens, J., I. Divnov, D. Adams, J. Murphy, and V. Bourchik (2002), Constraints on Infrasound Scaling and Attenuation Relations from Soviet Explosion Data, *Pure and Applied Geophysics* 159, 1045-1062.

Tolman, H., B. Balasubramaniyan, L. Burroughs, D. Chalikov, Y. Chao, H. Chen, and V. Gerald (2002), Development and Implementation of Ocean Surface Wave Models at NCEP, *Weather and Forecasting*, 17, 311-333.

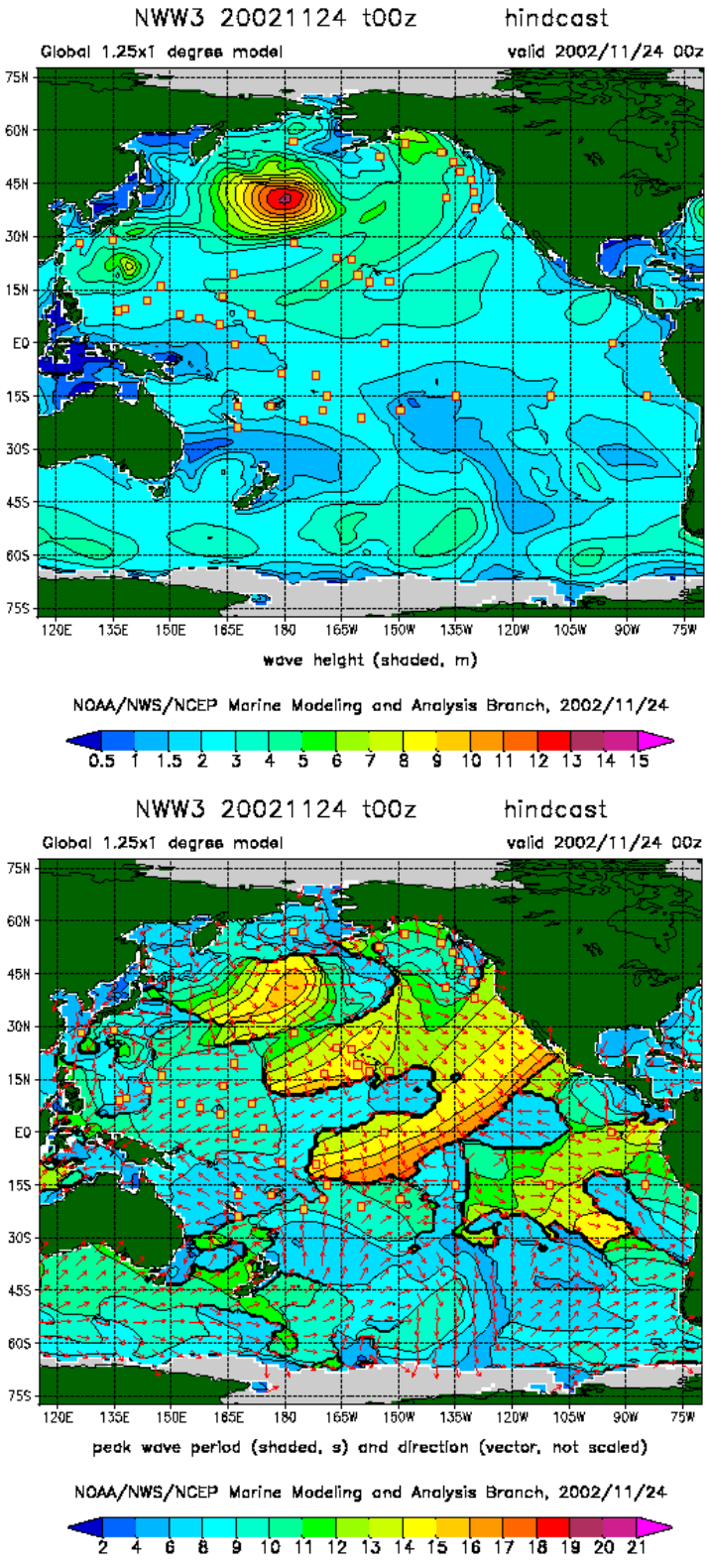

Figure 1. Significant wave height (upper panel) and dominant period and propagation direction for the global surface wave field on November 24, 2002 as predicted by WW3.

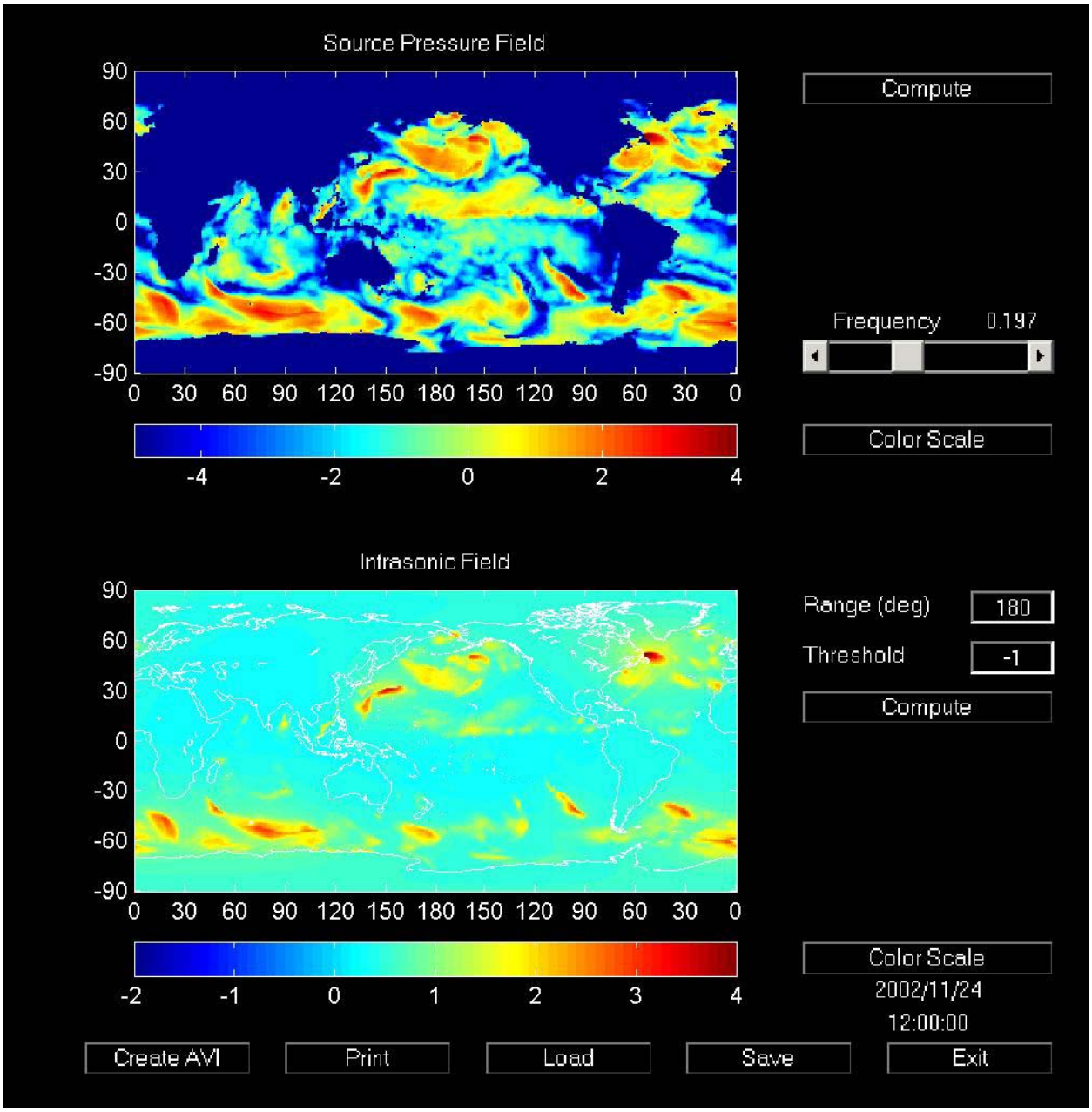

Figure 2. GUI panels showing the predicted source pressure field (top panel) and resultant infrasonic field (bottom panel) at a microbarom frequency of 0.2 Hz, as calculated from the output of WW3 for November 24, 2002. The infrasonic field results from a propagation limit of 180 degrees and a source magnitude cutoff of –1.

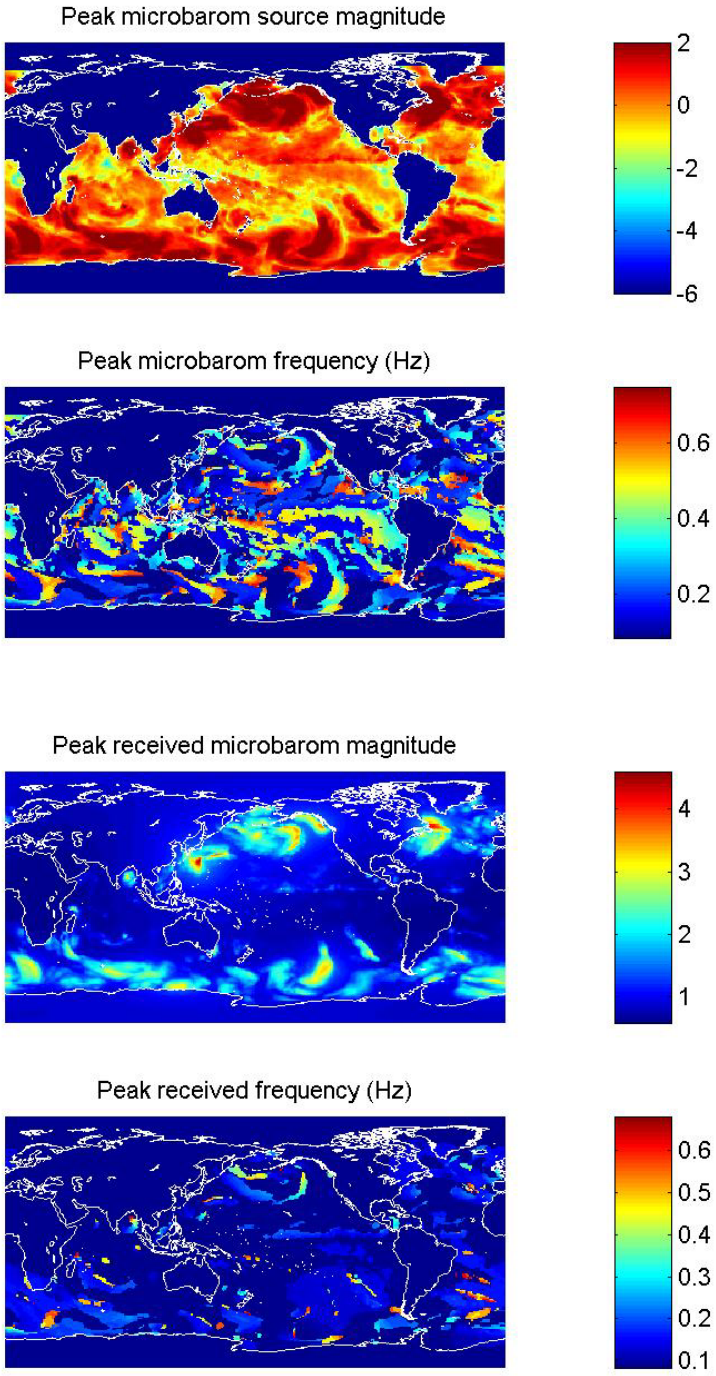

Figure 3. Panels showing peak source magnitude (top), the frequency at which the source peak magnitude occurs (second), peak received magnitude (third), and the frequency at which the received peak occurs (bottom) based on the results of WW3 for November 24, 2002.

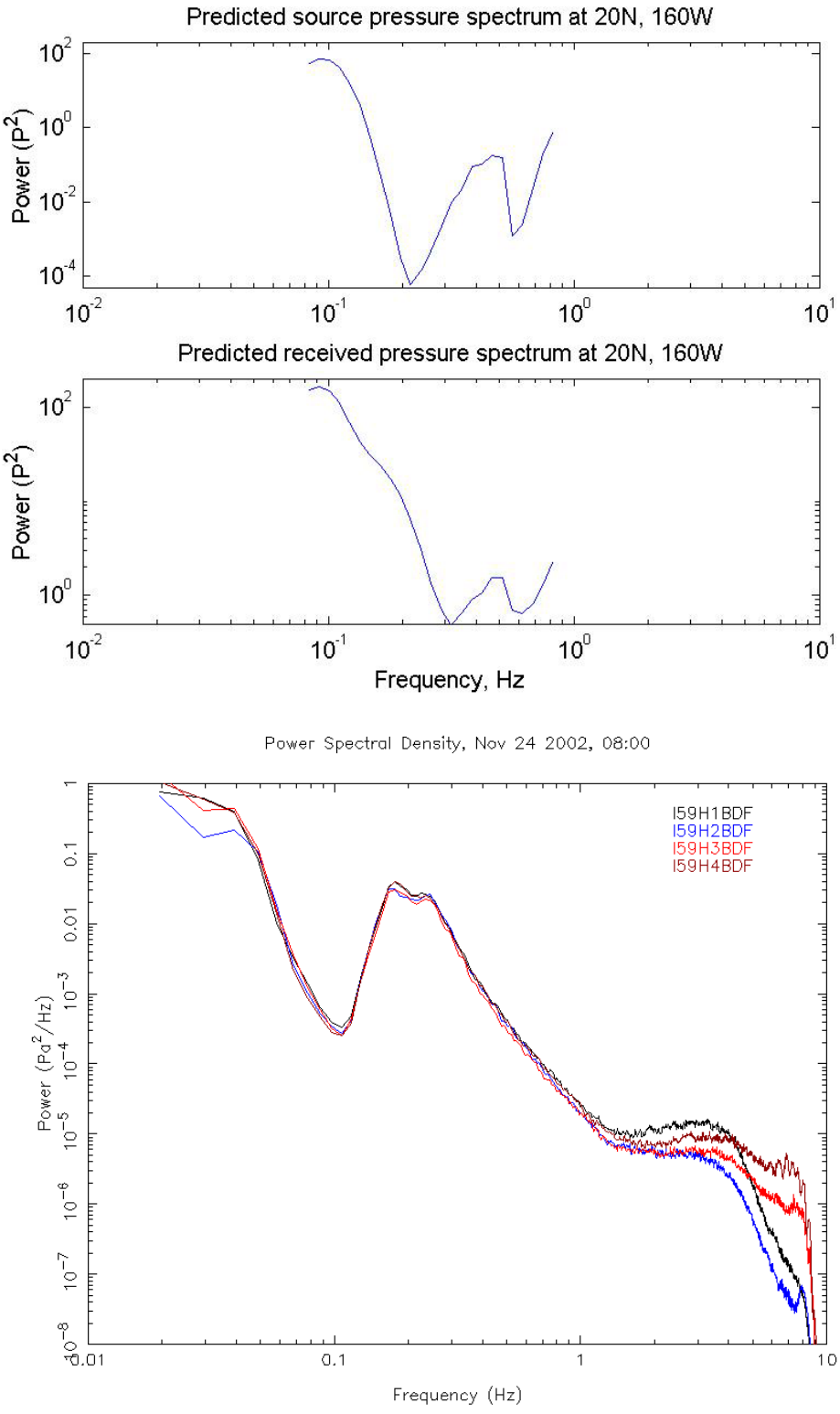

Figure 4. Predicted source pressure spectrum (top), predicted received pressure spectrum (middle) and observed pressure spectrum (bottom) for the Hawaii (20°N, 160°W) region on November 24, 2002.